RESEARCH ARTICLE

ADVANCED
SENSOR
RESEARCH
Open Access

www.advsensorres.com

On the Rational Design of Mesoporous Silica Humidity Sensors

*Máté Füredi, Alberto Alvarez-Fernandez, Maximiliano Jesus Jara Fornerod, Bálint Fodor, and Stefan Guldin**

Mesoporous silica is commonly used as matrix for humidity sensors which operate on the principle of relative humidity (RH)-dependent water uptake and read-out by resistance (R) monitoring. Although numerous studies have been dedicated to improving sensitivity with conductive additives, the role of the pore architecture on the sensing behavior has not been systematically investigated so far. Herein, the effects of pore size and porosity on resistive sensing performance in the 0.5–85% RH range are showcased. Across various sensors, a clear correlation is identified between mesopore size and linear RH sensing range. Sensors with larger pores ($\approx$15 nm) exhibit linear response in the 65 to 85% RH range with larger slope ($\Delta\log R/\Delta$RH) than sensors with smaller pores (<8 nm). Additionally, increasing porosity while retaining pore size, yields better overall sensor performance across the 15–85% RH range. In particular, a combination of pore size around 15 nm and porosity of 70% showcased a large resistance versus RH response ($R_0/R \approx 10000$) in the measured range, with quick response and recovery times of 3 and 9 seconds, respectively. These findings may serve as guidelines for developing broad spectrum high performance mesoporous sensors and for sensors specifically engineered to operate in specific RH ranges.

1. Introduction

Sensing relative humidity (RH) is a key feature in applications where moisture variation has an effect on performance (agriculture,[1,2] food processing,[3] electronics,[4] corrosion[5]), or where user comfort benefits from humidity control (automotive,[6] aviation,[7] smart home,[8] healthcare,[9]

M. Füredi, A. Alvarez-Fernandez, M. J. J. Fornerod, S. Guldin
Department of Chemical Engineering
University College London
Torrington Place, London WC1E 7JE, UK
E-mail: s.guldin@ucl.ac.uk
B. Fodor
Semilab Semiconductor Physics Laboratory Co. Ltd
4/A Prielle K. str., Budapest 1117, Hungary

and space vehicles industries[10]). Humidity sensors with a wide range, large sensing response, small hysteresis, rapid recovery, and low cost are the focus of research nowadays.[11] Typically, humidity sensing relies on changes in the physical properties of a material system when interacting with different amounts of gas phase water molecules, for example, changes in impedance,[12] piezoelectricity,[13] refractive index,[14] Bragg peak,[15] capacitance,[16,17] or electrical resistance[18,19] of the system. The last two examples, that is, resistive and capacitive sensors, represent the most used sensors in industrial applications due to their low cost and energy consumption, although they also display lower accuracy, compared to optical humidity sensors.[11]

In addition to full-range sensing, there is a growing interest in developing sensors with a high sensitivity for specific RH ranges.[20] While most commercial and industrial applications require monitoring and control of the RH within 40 and 60% for comfort and health effects,[21] other processes, such as fuel cell operation or microelectronic fabrication, are carried out in tightly controlled low RH environments.[22] Consequently, engineering humidity sensors for maximum performance in a narrow range allows more accurate control of RH in such applications. In this objective, the integration of nanostructured materials, such as nanoporous polymers,[23] metal-oxides,[24–28] or silica[28–32] has enabled the development of wide-range, high-performance sensors. The improvement in sensitivity[33] of mesoporous materials compared to their nonporous counterparts is related to the fact that mesoporous materials can adsorb atmospheric humidity well below saturation, changing the electrical properties of the sensing layer (see schematic in Figure S1, Supporting Information). The sensing mechanism typically follows four consecutive steps with increasing RH, which depend on pore size and surface functionalization: micropore filling, monolayer formation, multilayer adsorption, and finally capillary condensation. As such, the Kelvin equation provides a relationship between the RH at which capillary condensation occurs and the mesoscale pore size (2 to 50 nm).[34] Additionally, high accessible porosity and large surface area facilitate the protonic conduction of water.[35]

**ADVANCED
SCIENCE NEWS**

www.advancedsciencenews.com

**ADVANCED
SENSOR
RESEARCH**
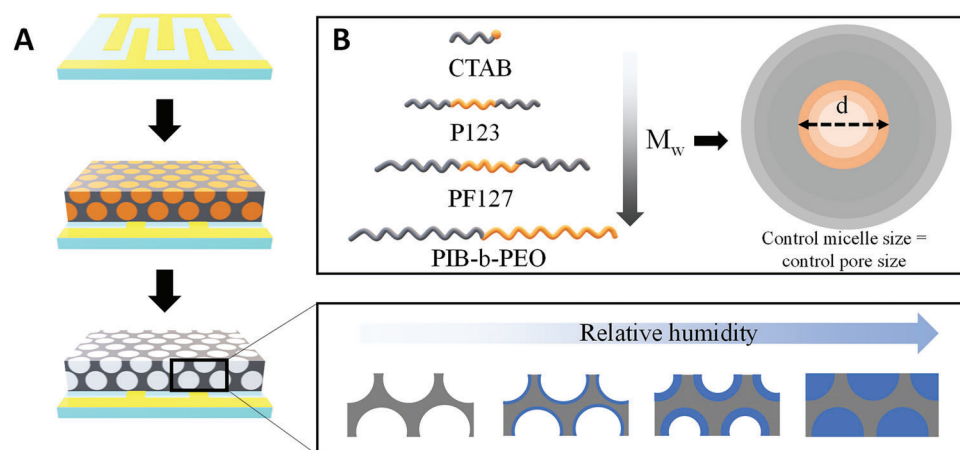
www.advsensorres.com

Figure 1. A) Mechanism of humidity sensing based on capillary condensation in the prepared the mesoporous films. B) Strategy toward the preparation of mesoporous humidity sensing layers with tuneable pore size and porosity (M_w: molecular weight of hydrophobic block, d: pore diameter).

While multiple fabrication methods have been studied to obtain porous inorganic materials for humidity sensing, such as etching of silicon,[36,37] aluminum,[38] and graphene,[39] most of these top-down approaches face challenges in their reproducibility, cost-effectiveness, and scalability. In contrast, the use of sol-gel chemistry enables facile bottom-up methods for preparing mesoporous silica with controlled architectures. Structure directing agents (SDAs), such as surfactants[40] and block copolymers (BCP)[41] can be used as template materials to prepare mesoporous materials with tunable porosities, pore sizes, and pore morphologies,[42–46] via co-assembly with inorganic precursors.

Mesoporous silica is one of the most versatile matrix materials for research of high-performance humidity sensors due to its low cost, ease of preparation, high surface area, and well-known surface chemistry.[47] Since the first studies introducing cetyltrimethylammonium bromide (CTAB) and poly(ethylene oxide)-poly(propylene oxide)-poly(ethylene oxide) (PEO-*b*-PPO-*b*-PEO) triblock copolymer templated mesoporous silica films as humidity sensors in the early 2000s,[33,48] co-assembly has become the standard fabrication strategy for silica-based humidity sensors. More recently, research efforts have been devoted to enhancing sensing performance of such matrices with dopants, such as Li,[29,30] Na,[49] K,[31] Ag,[50] or with nanocomposites, such as TiO$_2$,[51] and WO$_3$.[52] PEO-*b*-PPO-*b*-PEO is the most used BCP for co-assembly, typically as commercially available 'P123' or 'PF127'. Recent works have, however, demonstrated the preparation of mesoporous materials containing large mesopores (>10 nm) with diblock high-χ (highly amphiphilic with large Flory-Huggins parameter) BCP SDAs, such as poly(isobutylene)-*block*-poly(ethylene oxide) (PIB-*b*-PEO),[53] poly(isoprene)-*block*-poly(ethylene oxide) (PI-*b*-PEO)[54] or hydrogenated poly(butadiene)-*block*-poly(ethylene oxide) (PHB-*b*-PEO).[41]

To this end, the effect of mesoporous structure on sensing behavior has not been systematically studied yet. In early works of porous ceramic sensors, it was predicted that the sensing response is a direct function of the pore size distribution (PSD) based on the Kelvin-equation.[55] However, suitable preparation methods for inorganic architectures that facilitate detailed tuning of porosity and characteristic pore sizes over the full mesoscale

have only been established recently, via BCP co-assembly with varied SDA structural parameters.[41,53,54,56,57] This limitation, combined with the lack of adequate mesopore characterization tools has prevented the full validation of this hypothesis so far. In response, this work aims to establish a detailed structure-function relationship between pore architecture of mesoporous thin films and their resistive humidity sensing behavior by conducting a systematic study of multiple parameters. Unmodified mesoporous silica is chosen as model sensor for this work, as it serves as the fundamental material of several recently developed devices due to its chemical affinity to water and easy surface modification options for enhanced performance. We first fabricate mesoporous silica thin films using different SDAs—including a high-χ BCP not considered previously for RH sensing applications—to control the pore size (between 3 and 15 nm) and porosity (between 45% and 70%) of the material. We present environmental ellipsometric porosimetry (EEP) as a tool to correlate water uptake of sensing layers with changes in their electrical resistance (measured via direct current) upon RH change. A controllable RH chamber is used to benchmark sensors with ΔRH step sizes of $\approx$2.5% enabling near-continuous characterization of their electrical response. Finally, we demonstrate how independent manipulation of mesopore size and porosity enables tunable sensitivity across different RH ranges.

2. Results and Discussion

As previously introduced, two critical parameters in the fabrication of high-performance mesoporous humidity sensors are pore size and porosity. In order to establish a comprehensive and detailed study on the influence and impact of both parameters for the humidity sensing application, fine control over pore size (via sol-gel synthesis with different molecular weight SDAs) and porosity (via tuning SDA/material ratio) have been explored (**Figure 1**B). In a subsequent step, the resistive humidity-sensing performance of the different mesoporous thin films was studied following methodology shown in Figure 1A.
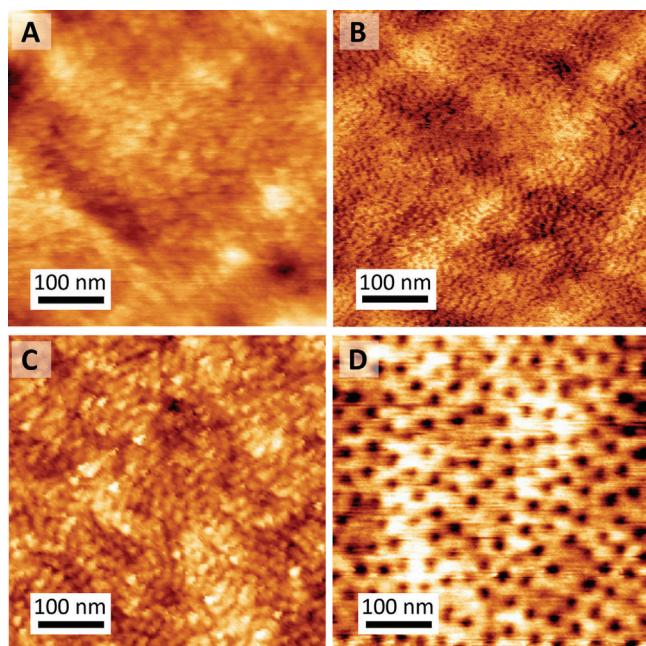
2200077 (2 of 11)

Figure 2. AFM micrographs of A) SiO_2-CTAB, B) SiO_2-P, C) SiO_2-PF, and D) SiO_2-PIB15 films.

2.1. Pore Size Manipulation for Tuned Sensitivity

Different SDAs, namely CTAB, PEO-b-PPO-b-PEO (in two different configurations referred to as P123 and PF127, respectively), and PIB-b-PEO, were used in the fabrication of mesoporous thin films with tunable pore sizes. Due to the variation in molecular weight (M_w) between the hydrophobic chains of different SDAs employed, inorganic mesoporous architectures with increasing pore dimensions were obtained.

Atomic force microscopy (AFM) topographic micrographs presented in **Figure 2** confirm the presence of a porous structure in all samples. However, limited information on pore sizes and porosities can be derived from samples obtained by the lower M_w SDAs (CTAB and P123), which may be related to the resolution limit of the tip and reveals some restrictions of surface imaging techniques for the characterization of mesoporous architectures.[58] In order to obtain precise information across the full range of porous architectures, environmental ellipsometric porosimetry was chosen as the standard characterization technique. **Figure 3**A–D presents the adsorption – desorption isotherms obtained by EEP of all mesoporous silica materials created using different SDAs. The PSD graphs corresponding to the volume adsorbed isotherms are shown in Figure 3E–H. Increases in the pore dimensions, related to the increment in the diameter of micelles formed by SDAs in solution, allowed pore size (diameter, D_{pore}) tuning between 3 and 15 nm, while keeping the porosity constant (47% ± 3%). All adsorption isotherms, corresponding to the four different SDA templated films, showed sharp increases in adsorbed volumes at characteristic relative pressure values, which is attributed to the capillary condensation of water in the mesopores.

A summary of the structural properties obtained by EEP is shown in Table S1, Supporting Information, including respective

film thicknesses and refractive indices. Notably, the total porosity and open porosity of the materials were in high correlation, demonstrating the good accessibility of prepared porous architectures toward water. As expected for mesoporous materials, the desorption curves showcased different behavior compared to adsorption. This hysteresis effect is usually attributed to the dimensions of interconnections between mesopores, however, the very late desorption in SiO_2-PF, and SiO_2-PIB15 templated silica may also be caused by cavitation.[59]

Since EEP uses water as adsorptive at room temperature instead of N_2 at 77 K in the commonly employed Brunauer–Emmett–Teller (BET)-porosimetry technique for bulk powders, it can present more relevant results for humidity sensors. Furthermore, the optical nature of the technique enables the study of porous films ranging from nm to µm thickness in a nondestructive and reliable way.[60] As neither volumetric nor gravimetric measurements of the adsorptive are carried out, the accuracy of measurement is independent of the quantity of the studied adsorbent film, which makes it especially suitable for thin film architectures deployed in humidity sensing.

To investigate the influence of pore size on the resistive sensor response, previously fabricated mesoporous thin films, with similar porosity and increasing pore size (SiO_2-CTAB, SiO_2-P, SiO_2-PF, and SiO_2-PIB15) were studied. Changes in the electrical resistance (R) of these sensing layers upon humidity variation are shown in **Figure 4**A–D and Figure S2A, Supporting Information.

We observed monotonously decreasing resistance with the increase of RH for all four sensors, where the resistance of the sensors at 85% RH was ≈10^4 times smaller than at 0.5% RH. This 4 orders of magnitude response (R_0/R across full measured RH range) is comparable to the $10^3 – 10^5$ response of other high-performance sensors from the past 5 years operating on resistance/current read-out.[52,61–64] All mesopore architectures displayed significant differences in their behavior across specific sections of the measured humidity range (0.5–85%), as visible in Figure 4.

The RH range where a sensor displays the largest slope of resistance decrease (highest sensitivity) is a crucial attribute for humidity sensing performance. For quantifying this, the local sensitivity ($d(\log R)/d(RH)$)- was defined[65] as the first derivative of the $\log R$–RH function (see Figure S2, Supporting Information). This allowed for a numerical comparison between sensing behaviors at different segments of the RH range. SiO_2-CTAB showcased a pronounced slope (higher local sensitivity) until 40% RH (see Figure 4A) with relatively good linearity of $\log R$ versus RH response, while the measured local sensitivity significantly decreased after 40% RH (see Figure 4B and Figure S2B, Supporting Information). In comparison, SiO_2-P exhibited near-perfect linear response between 10% and 60% RH (see Figure 4B) with decreased local sensitivity beyond this point. The sensing behavior of SiO_2-P at different RH ranges, and the overall ≈10^4 response was very similar to PEO-b-PPO-b-PEO-templated silica thin film sensors previously reported.[33,65] The "sensitivity cut-off"—outlined in the two examples above—coincided with the saturation of mesopores with water during EEP measurements. As shown in Figure 3, very little H_2O was adsorbed at higher RH than 45% in the small mesopores (≈3 nm) of the SiO_2-CTAB film, since most of them were completely filled at this point. The same
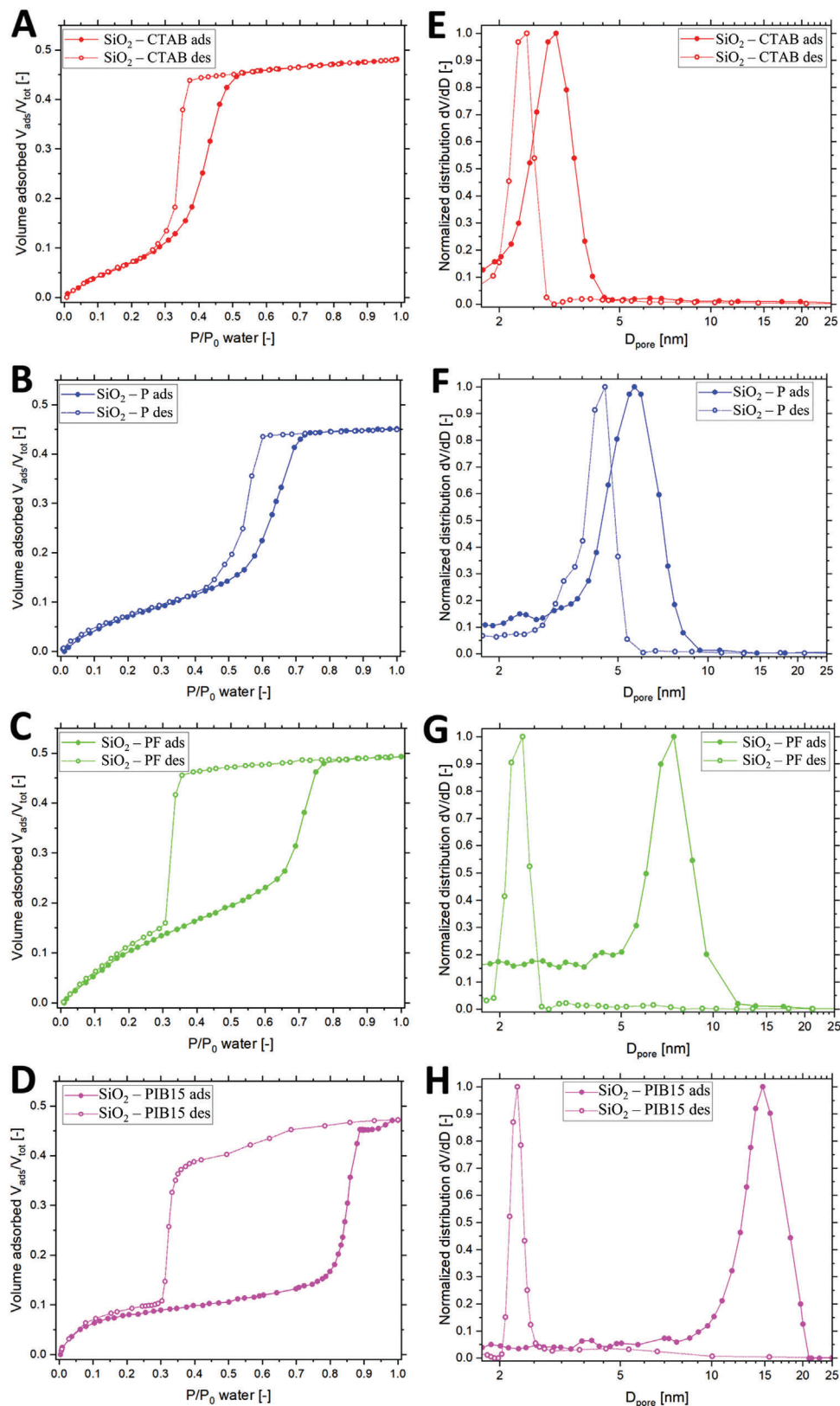
2200077 (3 of 11)

Figure 3. A–D) Volume adsorbed/desorbed ratio of water acquired by ellipsometric porosimetry and E–H) corresponding calculated pore diameter distributions for A,E) SiO₂-CTAB, B,F) SiO₂-P, C,G) SiO₂-PF, and D,H) SiO₂-PIB15 films.
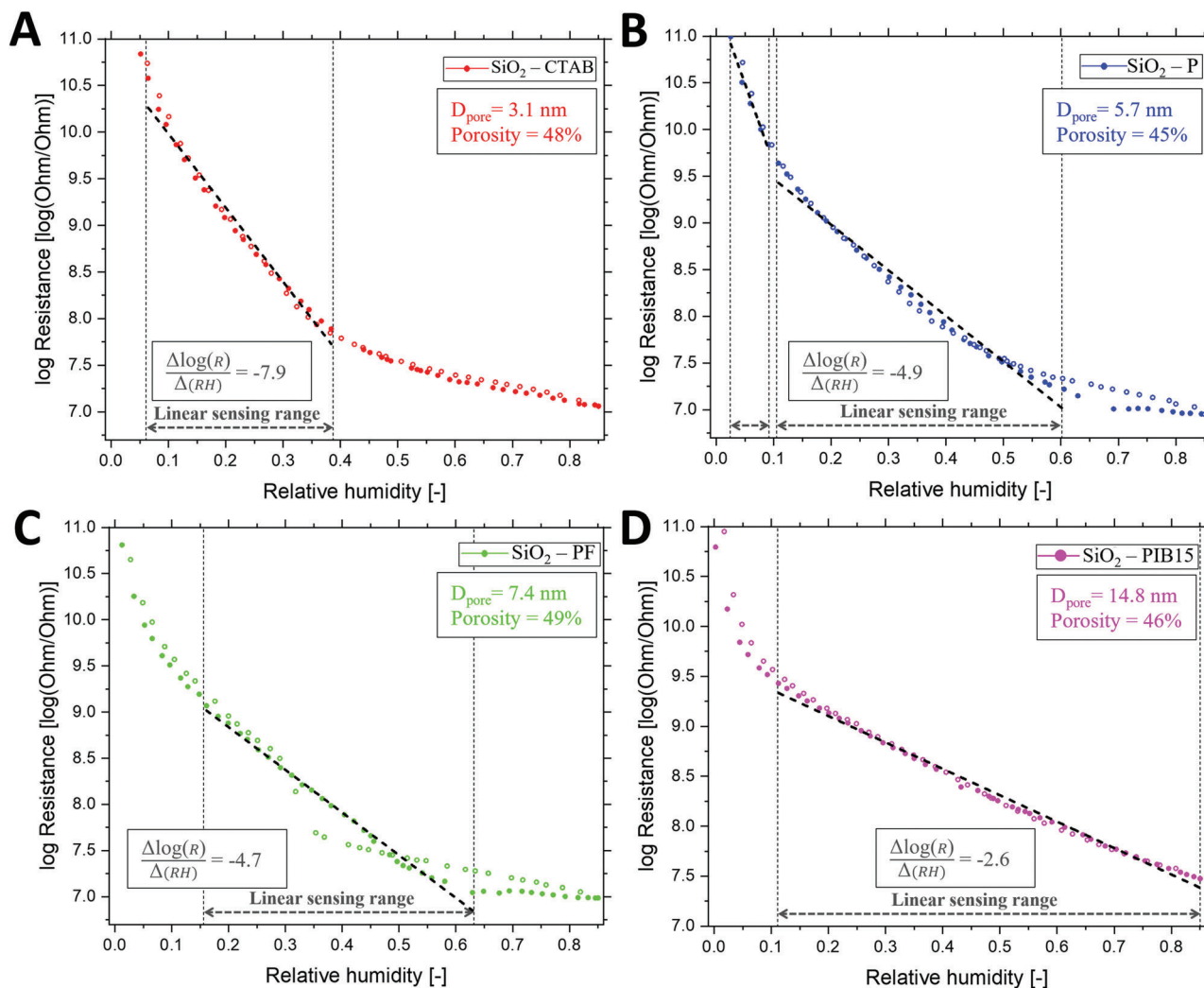
Figure 4. Electrical response versus RH plots for adsorption of sensors A) SiO_2-CTAB, B) SiO_2-P, C) SiO_2-PF, and D) SiO_2-PIB15, all possessing 47% ± 3% porosity, with linear fit in the linear sensing ranges (of adsorption) identified. Full and empty spheres represent data from increasing and decreasing RH cycles, respectively ($n = 1$).

explanation was found for the larger mesopores ($\approx$7 nm) in SiO_2-P material above 65% RH.

As shown in Figure 4C,D, Sensor SiO_2-PF revealed similar behavior as sensor SiO_2-P with a larger decrease of resistance at very low RH (<5%), while sensor SiO_2-PIB15 displayed a linear slope until high RH (85%) after a steep decline in resistance at very low RH (<5%). One possible explanation for the steep decline in resistance at low RH in the case of sensors SiO_2-PF and SiO_2-PIB15 is the presence of micropores that adsorb water at such low relative pressure range to form a conductive pathway in the films amenable to "proton hopping" even prior to monolayer formation. Previous reports have described the formation of micropores in other block-copolymer templated silica materials, which was attributed to hydrophilic PEO chains penetrating the silica matrix during film formation.[66–68] While PF127, P123, and PIB-b-PEO are all block copolymers with PEO components, it is worth noting that PF127 displays a higher volume fraction of ethylene-oxide compared to P123 (see Table S2, Supporting Information). Notably, we detected higher microporous adsorption in

the cases of sensors SiO_2-PIB15 and SiO_2-PF when compared to sensors SiO_2-CTAB and SiO_2-P, which further supports our hypothesis (see Figure 3 below 0.15 P/P_0). Based on these results, high-χ BCP templated silica sensors can be deemed superior for broad spectrum RH sensing, as they enable the incorporation of larger mesopores (>10 nm) into the matrix. One example of these showcased in this work, PIB-b-PEO templated silica (SiO_2-PIB15) exhibited the widest linear range (see Figure 4D and Figure S2, Supporting Information) and the largest low RH (<5%) local sensitivity out of the 47% ± 3% porosity sensors investigated in this section, owing to its hierarchical structure of micropores and large mesopores.

Response and recovery times were calculated based on the fitting described in the Supporting Information. Response times of $\approx$3–4 s were observed in all sensors (Table S3, Supporting Information). For sensors SiO_2-CTAB and SiO_2-P, we observed rapid recovery times of 7 s and 5 s, respectively. In comparison, sensors SiO_2-PF and SiO_2-PIB15 exhibited much slower recovery (30 s and 53 s, respectively). Based on changes in pore size alone, no
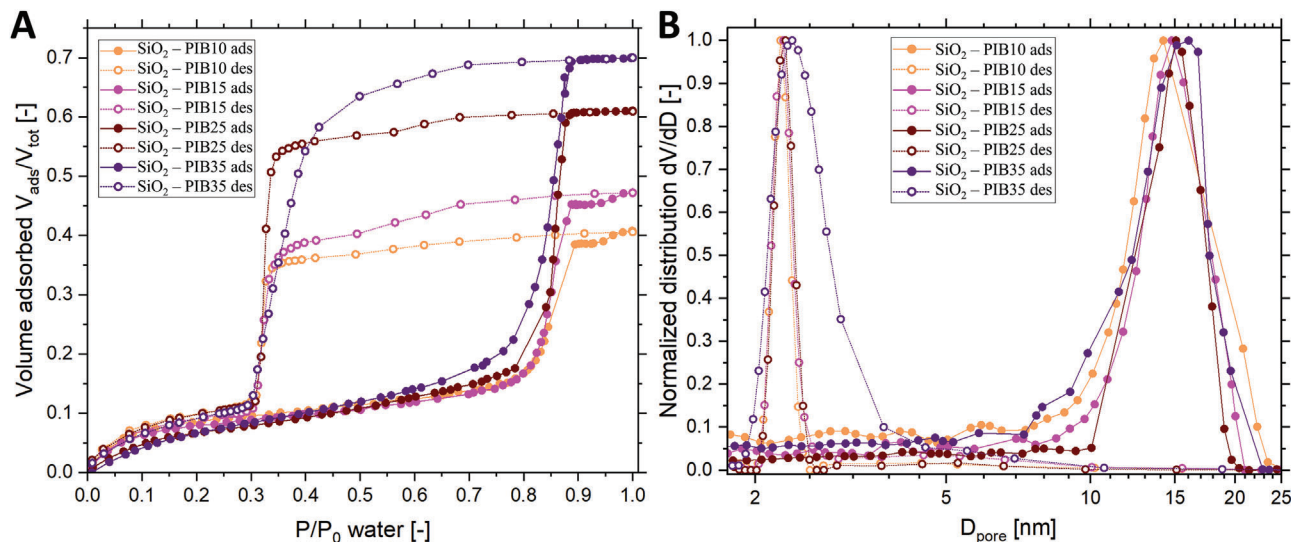
Figure 5. A) Volume adsorbed/desorbed ratio of water acquired by ellipsometric porosimetry and B) calculated PSD of SiO$_2$-PIB films prepared from precursor sols containing nominally 10%, 15%, 25%, and 35% organic SDA weight ratios.

correlations could be drawn regarding recovery behavior, indicating more significant effects of other parameters such as micro- and mesoporosity. These are discussed in detail in the next section.

2.2. Porosity Manipulation for Tuned Sensitivity

To study the effect of porosity on the resistance response to humidity, we prepared films with similar pore size and different porosities. PIB-*b*-PEO was selected due to the promising performance of sensor SiO$_2$-PIB15 discussed previously. **Figure 5** exhibits EEP isotherms of PIB-*b*-PEO templated silica sensors prepared using varying template:material (organic:inorganic) mass ratios.

The similarity of isotherms confirmed that it was possible to tune the final porosity of the film (between 40% and 70%) while keeping the pore size nearly constant. Grazing incidence small angle X-ray scattering (GISAXS) measurements (shown in Figure S4, Supporting Information) confirm the decrease in the center-to-center pore distances with increasing SDA content, indicating a thinner pore wall thickness for the more porous sensors.

To study the effect of porosity on the resistance response of the sensors, SiO$_2$-PIB samples with tuned porosity values were investigated. The resistance response and linear range are shown in **Figure 6**A–D for sensors SiO$_2$-PIB10, SiO$_2$-PIB15, SiO$_2$-PIB25, and SiO$_2$-PIB35. We observed that the obtained microporosity, i.e. pores <2 nm, was inversely proportional to the amount of SDA used in the fabrication of the films (Figure 5).

To verify this observation, we characterized the samples using vacuum ellipsometric porosimetry with methanol as adsorptive (see Figure S5, Supporting Information). Based on methanol adsorption, 10 w% of SDA resulted in ≈9.5 vol% microporosity, while using 35 w% SDA led to only ≈6.5 vol%. Previous

studies have observed increased microporosity with higher material:template ratio in the case of PEO-*b*-PPO-*b*-PEO templated silica. This effect was attributed to stress-induced defects in pore walls caused by PEO chains, which give way to more micropores (i.e., defects) in the case of lower porosity (higher wall thickness).[69] Our results are consistent with a similar phenomenon in the high-χ BCP templated silica humidity sensors studied herein, which in turn also influences sensing behavior in the <5% RH range. This is in line with the aforementioned GISAXS measurements (Figure S4, Supporting Information), providing evidence of increasing wall thickness for sensors prepared using lower SDA content. While the local sensitivity below 5% RH was found lower in the case of SiO$_2$-PIB sensors prepared with larger SDA content, in the 15% < RH < 85% range, those samples displayed higher local sensitivity (see Figure S3, Supporting Information). Our findings demonstrate the role of micro-, and mesoporosity (at constant pore size) on the humidity sensing response in different RH ranges. We also note the reproducibility of the herein fabricated humidity sensors, with samples made from identical recipes but different batches displaying consistent behavior (see Figures S6 and S7, Supporting Information).

The resistance response/recovery behavior of SiO$_2$-PIB sensors is depicted in **Figure 7**. Enabled by good pore accessibility, with all sensing layers prepared in this work of submicron thickness (between 100 and 300 nm, see Table S1, Supporting Information), all measured response times were quick (<5 s) due to near-instantaneous capillary condensation across the whole porous film layer. Sensors SiO$_2$-PIB35, SiO$_2$-PIB25, SiO$_2$-PIB15, and SiO$_2$-PIB10 showed monotonously increasing recovery times (9, 37, 53, 80 s). This trend correlates with the decrease in sensor meso- and increase in sensor microporosities. It is worth noting, that the less microporous sensors SiO$_2$-CTAB and SiO$_2$-P also exhibited quicker recovery (7 s and 5 s respectively) than the more microporous SiO$_2$-PF (30 s), as shown in
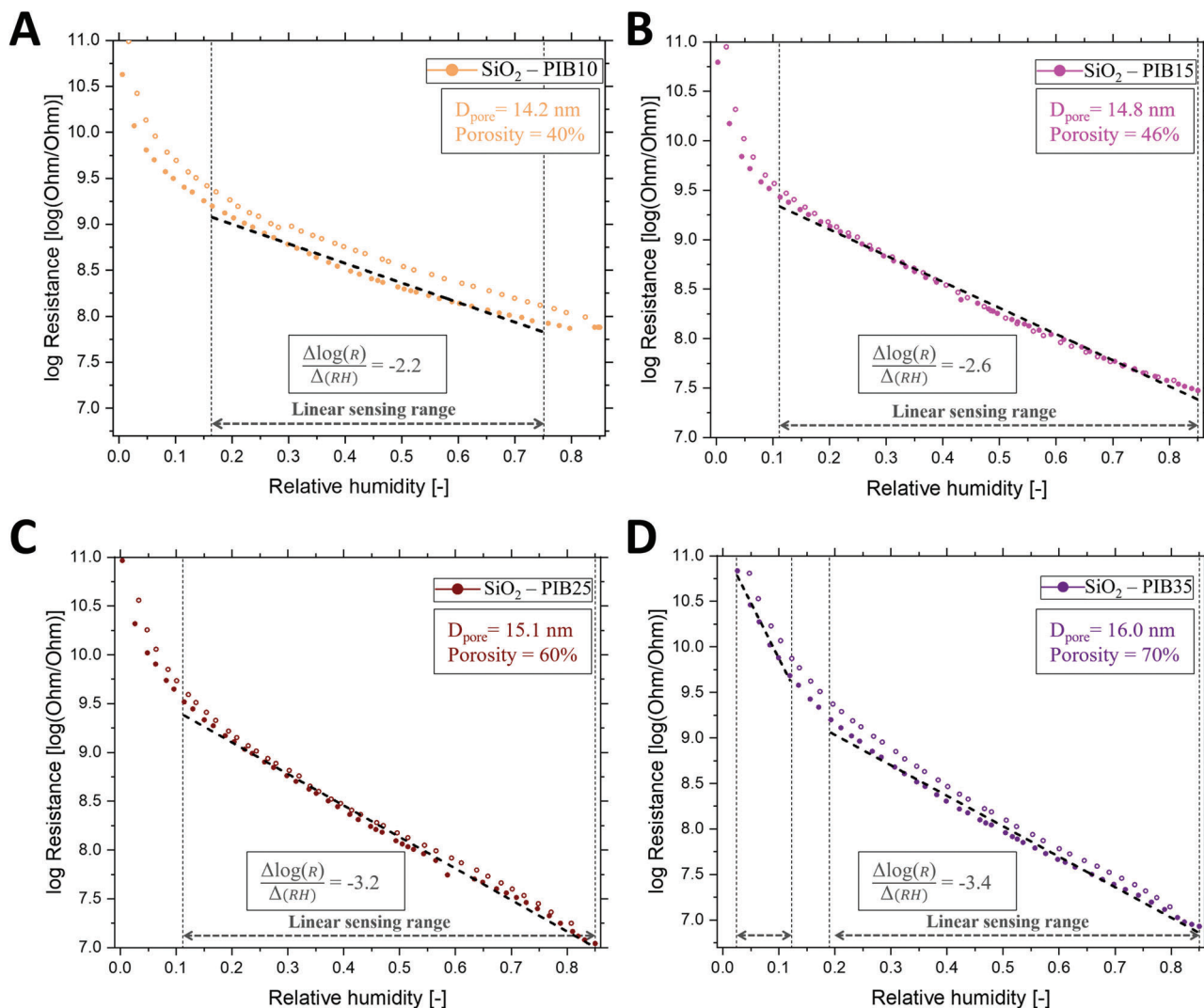
Figure 6. Electrical response versus RH plots for adsorption of sensors A) SiO$_2$-PIB10, B) SiO$_2$-PIB15, C) SiO$_2$-PIB25, and D) SiO$_2$-PIB35 with linear fit in the linear sensing ranges (of adsorption) identified. Full and empty spheres represent data from increasing and decreasing RH cycles respectively ($n = 1$).

Table S3, Supporting Information. All these results provide evidence of a correlation between microporosity in a sensing layer and slower recovery behavior.

2.3. Sensor Design Guidelines: Toward the Optimal Design

The results discussed in the previous sections provide guidance toward the rational design of mesoporous sensors for maximum resistance response in the desired RH ranges. We attribute the main structural factors of porous architectures determining sensing behavior to microporosity, mesoporosity, and pore size. Our findings build on the pioneering work of K.-S. Chou et al.,[70] who reported that specific surface area is the major contributor toward high sensitivity at 10–20% RH, while porosity and capillary condensation plays the key role at higher RH (>80%). At ranges where specific surface area determines sensitivity, electrical con-

nection is enabled by proton-hopping through Si-OH groups which can proceed with very small amount of adsorbed water through hydrogen bonding.[35,71] At higher RH values, a larger amount of water is adsorbed based on multilayer adsorption—and eventually capillary condensation-, which enables greater conductance through hydronium ions.[49] Our results show that the sensitivity of the prepared sensors across the humidity ranges is influenced by their porous characteristics, namely microporosity, specific surface area, mesoporosity, and pore size.

Based on our analysis of the local sensitivity functions, the two sensors with the largest microporosity, templated by PF127 (SiO$_2$-PF) and 15% PIB-*b*-PEO (SiO$_2$-PIB15) were the most sensitive below 5% RH.

For applications operating in relatively narrow RH range between 10% and 40%, CTAB-templated silica sensors (SiO$_2$-CTAB) offer higher performance and better linearity than the higher molecular weight block polymer-templated sensors investigated

ADVANCED
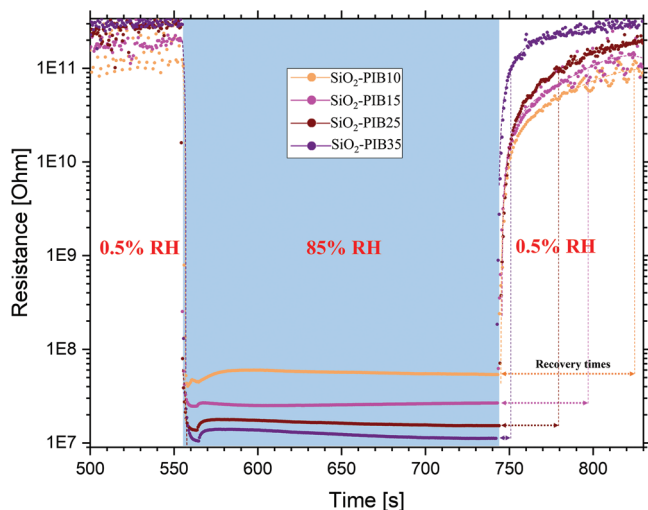**SCIENCE NEWS**

www.advancedsciencenews.com

ADVANCED
SENSOR
RESEARCH
Open Access

www.advsensorres.com

Figure 7. Response/recovery behavior of SiO$_2$-PIB sensors.

in this work (see Figure 4). The small (≈3 nm) mesopores of SiO$_2$-CTAB were almost entirely filled up with water by 45% RH by capillary condensation, which we relate as the cause of its high local sensitivity in the lower RH range. This sensor also exhibited higher specific surface area (SSA) than block copolymer-templated sensors (see Table S3, Supporting Information) highlighting the SSA-controlled sensitivity mechanism in this RH range as described above.

The PEO-*b*-PPO-*b*-PEO templated sensors (SiO$_2$-P and SiO$_2$-PF) were found to be most sensitive between 35 and 65% RH with good linearity. This compares to SiO$_2$-CTAB sensors, which have already reached their saturation water content at these levels of RH and SiO$_2$-PIB sensors, where the larger mesopores adsorb smaller relative amounts of water (see Figure 3) in this range.

SiO$_2$-PIB sensors showcased good linearity in the 15–65% range, furthermore their local sensitivity can be significantly improved by increasing the porosity (SiO$_2$-PIB25 and SiO$_2$-PIB35 sensors). This increment in porosity corresponds to a larger pore volume, where gradual multilayer adsorption can occur, resulting in a higher water uptake. This effect is visible in both EEP (Figure 5) and sensing response (Figure 6), which are in close correlation with each other. These sensors do not reach pore filling until 85% due to their larger pores (≈15 nm), making them superior for sensing in the high RH (>65%) range while also offering best overall linearity in the widest RH range (15–85%). We want to emphasize the role of microporosity in the response/recovery times. The less microporous sensors discussed in this work, SiO$_2$-CTAB, SiO$_2$-P, and SiO$_2$-PIB35, are comparable to state of the art of silica-based humidity sensors reported the last 5 years.[52,64,71,72] while sensors with higher microporosity (e.g., SiO$_2$-PF and SiO$_2$-PIB15) exhibited slower response.

We further note that the sensor design guidelines presented in this paper are applicable to other micro-/mesoporous matrices, which might be exploited due to the inherent limitations of silica with regard to mechanical resistance[73] and long-term stability.[74,75] The outline of this study may also be used for future works regarding humidity sensors with different read-out mechanisms, such as impedimetric, capacitive, or gravimetric means.

3. Conclusions

In summary, a series of mesoporous silica resistive humidity sensors with tuneable pore size, interpore distances, and porosity were fabricated using co-assembly with different SDAs. In terms of structural characterization, EEP proved to be a powerful characterization tool for humidity sensors for uncovering structure-sensing behavior relationships. With regard to sensing performance, the pore size revealed to be a critical parameter to control sensor's linear response range. For sensors with similar porosity (47 ± 3%), larger pore sizes (≈15 nm) showcased a wider linear response (15% to 85% RH) than smaller pore sizes. The effect of porosity was also explored, with increased mesoporosity (to 60% or above) offering improved sensitivity and linearity, while enhanced microporosity, linked to the use of a lower amount of SDA, provided improved performance at very low RH (<5%). Hence, we demonstrate that pore size and porosity are two key structural parameters in the performance of silica-based resistive humidity sensors, with detailed tuning required for optimum operation across a target range. Future studies should aim to develop hierarchical architectures for optimum operation across the full RH range. The development of application-specific high performance humidity sensors based on a wide range of surface chemistries will benefit from the discussed rationally designed porous architectures.

4. Experimental Section

Chemicals: Chemicals were used without further purification. Tetraethyl-orthosilicate (TEOS, >99%) was purchased from Sigma. Ethanol (99.8%) was purchased from Fischer. MilliQ water was used where stated. Hydrochloric acid (37%) was purchased from Merck. CTAB (>99%) was purchased from Sigma. PEO$_{106}$-PPO$_{70}$-PEO$_{106}$ (PF127) and PEO$_{20}$-PPO$_{70}$-PEO$_{20}$ (P123) powders were purchased from Sigma. PIB$_{39}$-PEO$_{36}$ was supplied by BASF.

Preparation of Mesoporous Silica Materials: Mesoporous silica materials were prepared using the following SDAs (see Table S2, Supporting Information).

CTAB/Compound Templating: 2.08 g TEOS was mixed with 2.218 mL ethanol, with the subsequent dropwise addition of 0.901 mL (pH = 1.33) hydrochloric acid. This sol was aged at 40 °C for 4 h before adding sufficient CTAB/ethanol solution to reach 0.14 CTAB/TEOS molar ratio (as reported elsewhere).[76] P123 as a co-surfactant was added in this step in a 0.02 P123/TEOS molar ratio. The combined use of P123 and CTAB was reported to possess improved properties.[77] Because of the very high (≈35) CTAB/P123 molar ratio used in this case, the thus prepared films are denoted as "SiO$_2$-CTAB" in the text.

PEO-b-PPO-b-PEO Templating: 4.5 g TEOS was mixed with 2.363 mL ethanol. 2.138 mL 10 mM hydrochloric acid was added dropwise to create a precursor sol with nominally 1000 mg mL^{-1} inorganic silica concentration. The sol was stirred at room temperature for 3 h before transferring 0.360 mL to a new vial and mixing with ethanolic solution of either 0.900 mL (50 mg mL^{-1}) P123 or 0.576 mL (103.6 mg mL^{-1}) PF127. The thus prepared films are denoted in the text as "SiO$_2$-P" for the P123 templated material or "SiO$_2$-PF" for PF127 templated material.

PIB-b-PEO Templating: 4.5 g TEOS was mixed with 2.363 mL ethanol. 2.138 mL 10 mM hydrochloric acid was added dropwise to create a precursor sol with nominally 1000 mg mL^{-1} inorganic silica concentration. The sol was stirred at room temperature for 3 h before pipetting and transferring 0.360 mL to a new vial and mixing with ethanolic solution of 0.636 mL (50 mg mL^{-1}) PIB-*b*-PEO for a 15% nominal organic mass ratio. Various template/silica sol ratios were prepared by modifying the PIB-*b*-PEO solution added (the nominal SDA/material mass percentage varied

**ADVANCED
SCIENCE NEWS**

www.advancedsciencenews.com

**ADVANCED
SENSOR
RESEARCH**

www.advsensorres.com

from 10% to 35%). The thus prepared films are denoted in the text as "SiO$_2$-PIB10," "SiO$_2$-PIB15," "SiO$_2$-PIB25," and "SiO$_2$-PIB35" based on the nominal SDA content used.

Fabrication of Transparent Humidity Sensors: The mixtures were immediately spin-coated at 5000 rpm onto silicon and interdigitated indium tin oxide coated glass substrates (Ossila Ltd, 20 × 15 mm, electrode thickness: 100 nm, distance between electrodes 50 μm) respectively. For removing the organic SDAs and the complete condensation of the inorganic precursor, the samples were calcined in a muffle furnace at 450 °C for 30 min (5 °C min^{-1} ramping speed).

Humidity Sensing Measurements: The change in electrical resistance of the sensors upon exposure to humidity was measured by a Keithley 2450 source measure unit. A sufficiently high bias voltage of 10 V with 10 s wait times was selected to minimize any effects of polarization,[78] and improve measurement accuracy at the low RH range.[71] In contrast to the common benchmarking of humidity sensors by measuring their resistance at 5 or 6 points of RH (e.g., 11, 33, 54, 78, 98%) via saturated salt solutions,[79–81] a chamber was utilized, in which RH (at a fixed temperature) was continuously controllable across the spectrum without the need to remove the benchmarked sensor between measurement steps. 40 individual RH steps were set in the range between 0.5 and 85% by controllable flows of dry N$_2$, and wet air (with saturated level of H$_2$O vapor) intake. With each measurement cycle the aim was to establish a near-continuous function of the resistance-RH relationship. All measurements were carried out at room temperature (25 °C). Samples were treated with oxygen plasma for 300 s to remove residual organic contaminants inside the pores, and subsequently subjected to 30 min of constant bias voltage before commencing measurements.

Material Characterization: Ellipsometric porosimetry (EP) measurements were carried out on a Semilab SE-2000 spectroscopic ellipsometer (within the spectral range of 300 to 900 nm) with humidity and vacuum chamber extensions for measurements with water and methanol adsorptives respectively. All ellipsometric data analysis was performed with SEA software using Cauchy dispersion model fitting. For the environmental ellipsometric porosimetry and vacuum ellipsometric porosimetry measurements, thin films spin-coated from the same sol onto silicon wafers were studied due to the better reliability of obtaining ellipsometric spectra of thin films deposited on absorbing substrates. During EP measurements, ellipsometric spectra were recorded stepwise at 30 P/P_0 steps (in the range between 0.5 and 100%) to obtain the adsorption and desorption isotherms from the fitted refractive index values. The set RH doses were achieved via the integrated closed humidity chamber with controllable nitrogen and air with saturated level of H$_2$O vapor (dry and wet gas) intake. The modified Kelvin-equation was used to obtain mesopore size distribution information as described previously.[82] Measurements with methanol adsorptive were analogously carried out in a vacuum chamber enabling precise control of relative adsorptive pressure. Prior to all EP measurements, samples were treated with oxygen plasma for 300 s to remove residual organic contaminants inside the pores. Lorentz-Lorenz effective medium approximation (EMA) was utilized to model the refractive index of porous solids partially filled with air and adsorptive molecules.[83,84] Ellipsometric spectra acquired at different relative pressures of the adsorptive were used to construct volume adsorbed isotherms. Porosity was calculated using the Lorentz-Lorenz EMA for the adsorptive filled porous layer at $P/P_0 = 1$, while specific surface area was derived via the classical BET-fitting on the obtained isotherms.[58,85,86]

Atomic force microscopy was used to capture the surface morphology of prepared mesoporous silica samples. AFM images were obtained on a Bruker Dimension Icon atomic force microscope with a SCOUT350 (Nunano, UK) probe (nominal tip radius 5 nm) in tapping mode.

Grazing incidence small angle X-ray scattering measurements were performed to gather information on center-to-center pore distance. Measurements were carried out at the Centre de Recherche Paul Pascal at Université de Bordeaux using a high-resolution X-ray spectrometer Xeuss 2.0 (Xenocs) operating with radiation wavelength of 1.54 Å. 2D scattering patterns were collected using a PILATUS 300K Dectris detector with a sample-to-detector distance of 1188 mm. The beam center position and the angular range were calibrated using a silver behenate standard

sample. GISAXS data analysis was accomplished with the FitGISAXS software.[87]

Statistical methods used in this work are shown in Figures S6 and S7, Supporting Information (reproducibility testing). For sample sizes of n = 2, mean measurement values were plotted complemented by error bars (of standard deviation). The exact sample size in all cases (n = 1 or 2) is reported in corresponding figure captions.

Supporting Information

Supporting Information is available from the Wiley Online Library or from the author.

Conflict of Interest

The authors declare no conflict of interest.

Data Availability Statement

The data that support the findings of this study are available from the corresponding author upon reasonable request.

[1] M. Srbinovska, C. Gavrovski, V. Dimcev, A. Krkoleva, V. Borozan, *J. Cleaner Prod.* **2015**, *88*, 297.

[2] R. N. Dean, A. K. Rane, M. E. Baginski, J. Richard, Z. Hartzog, D. J. Elton, *IEEE Trans. Instrum. Meas.* **2012**, *61*, 1105.

[3] N. Benabdellah, M. Bourhaleb, M. Nasri, N. Benazzi, S. Dahbi, in *Design of Temperature and Humidity Sensors for an Electronic Nose Used in Rotten Food*, IEEE, Piscataway, NJ **2016**, pp. 505-509.

[4] J. Cai, C. Lv, E. Aoyagi, S. Ogawa, A. Watanabe, *ACS Appl. Mater. Interfaces* **2018**, *10*, 23987.

[5] B. Raju, R. Kumar, M. Senthilkumar, R. Sulaiman, N. Kama, S. Dhanalakshmi, *Sustainable Energy Technol. Assess.* **2022**, *52*, 102306.

[6] B. Patissier, *Sens. Actuators, B* **1999**, *59*, 231.

[7] S. Mondal, B. K. Min, Y. Yi, C. Choi, *Adv. Mater. Technol.* **2022**, *7*, 2100751.

[8] W. A. Jabbar, M. H. Alsibai, N. S. S. Amran, S. K. Mahayadin, in *2018 International Symposium on Networks, Computers and Communications (ISNCC)*, IEEE, Piscataway, NJ **2018**, pp. 1–6.

[9] Y. Ma, S. Ma, T. Wang, W. Fang, *Sens. Actuators, A* **1995**, *49*, 47.

[10] M. A. Ryan, H. Zhou, M. G. Buehler, K. S. Manatt, V. S. Mowrey, S. P. Jackson, A. K. Kisor, A. V. Shevade, M. L. Homer, *IEEE Sens. J.* **2004**, *4*, 337.

[11] S. Sikarwar, B. C. Yadav, *Sens. Actuators, A* **2015**, *233*, 54.

[12] J. Wang, M. Y. Su, J. Q. Qi, L. Q. Chang, *Sens. Actuators, B* **2009**, *139*, 418.

[13] S. Mintova, S. Mo, T. Bein, *Chem. Mater.* **2001**, *13*, 901.

[14] S. Muto, O. Suzuki, T. Amano, M. Morisawa, *Meas. Sci. Technol.* **2003**, *14*, 746.

[15] F. Gallego-Gómez, M. Morales, A. Blanco, C. López, *Adv. Mater. Technol.* **2019**, *4*, 1800493.

[16] U. Kang, K. D. Wise, *IEEE Trans. Electron Devices* **2000**, *47*, 702.

[17] E. Zampetti, S. Pantalei, A. Pecora, A. Valletta, L. Maiolo, A. Minotti, A. Macagnano, G. Fortunato, A. Bearzotti, *Sens. Actuators, B* **2009**, *143*, 302.

[18] K. P. Yoo, L. T. Lim, N. K. Min, M. J. Lee, C. J. Lee, C. W. Park, *Sens. Actuators, B* **2010**, *145*, 120.

[19] G. Montesperelli, A. Pumo, E. Traversa, Gusmano, A. B., A. Montenero, G. Gnappi, *Sens. Actuators, B* **1995**, *25*, 705.

[20] L. A. Currie, *Pure Appl. Chem.* **1995**, *67*, 1699.

[21] L. Alwis, T. Sun, K. T. V. Grattan, *Measurement* **2013**, *46*, 4052.

[22] Y. Wang, *J. Electrochem. Soc.* **2009**, *156*, B1124.

[23] I. Fratoddi, A. Bearzotti, I. Venditti, C. Cametti, M. V. Russo, *Sens. Actuators, B* **2016**, *225*, 96.

[24] S. Blessi, A. Manikandan, S. Anand, M. M. L. Sonia, V. M. Vinosel, A. M. Alosaimi, A. Khan, M. A. Hussein, A. M. Asiri, *Phys. E* **2021**, *133*, 114820.

[25] Y. Zhu, J. Chen, H. Li, Y. Zhu, J. Xu, *Sens. Actuators, B* **2014**, *193*, 320.

[26] S. P. Gupta, A. S. Pawbake, B. R. Sathe, D. J. Late, P. S. Walke, *Sens. Actuators, B* **2019**, *293*, 83.

[27] V. K. Tomer, S. Duhan, *Sens. Actuators, B* **2016**, *223*, 750.

[28] L. Almar, A. Tarancón, T. Andreu, M. Torrell, Y. Hu, G. Dezanneau, A. Morata, *Sens. Actuators, B* **2015**, *216*, 41.

[29] T. Zhang, R. Wang, W. Geng, X. Li, Q. Qi, Y. He, S. Wang, *Sens. Actuators, B* **2008**, *128*, 482.

[30] W. Geng, R. Wang, X. Li, Y. Zou, T. Zhang, J. Tu, Y. He, N. Li, *Sens. Actuators, B* **2007**, *127*, 323.

[31] W. Zhang, R. Wang, Q. Zhang, J. Li, *J. Phys. Chem. Solids* **2012**, *73*, 517.

[32] T. Wagner, S. Krotzky, A. Weiß, T. Sauerwald, C.-D. Kohl, J. Roggenbuck, M. Tiemann, *Sensors* **2011**, *11*, 3135.

[33] A. Bearzotti, J. M. Bertolo, P. Innocenzi, P. Falcaro, E. Traversa, *J. Eur. Ceram. Soc.* **2004**, *24*, 1969.

[34] J. Shah, R. K. Kotnala, B. Singh, H. Kishan, *Sens. Actuators, B* **2007**, *128*, 306.

[35] F. Ernsberger, *J. Am. Ceram. Soc.* **1983**, *66*, 747.

[36] E. J. Connolly, G. M. O'Halloran, H. T. M. Pham, P. M. Sarro, P. J. French, *Sens. Actuators, A* **2002**, *99*, 25.

[37] G. Korotcenkov, E. Rusu, *Phys. Status Solidi A* **2019**, *216*, 1900348.

[38] K. Sharma, S. S. Islam, *Sens. Actuators, B* **2016**, *237*, 443.

[39] Y. Pang, J. Jian, T. Tu, Z. Yang, J. Ling, Y. Li, X. Wang, Y. Qiao, H. Tian, Y. Yang, T.-L. Ren, *Biosens. Bioelectron.* **2018**, *116*, 123.

[40] D. Grosso, F. Cagnol, G. J. de, A. A. Soler-Illia, E. L. Crepaldi, H. Amenitsch, A. Brunet-Bruneau, A. Bourgeois, C. Sanchez, *Adv. Funct. Mater.* **2004**, *14*, 309.

[41] M. Stefik, J. Song, H. Sai, S. Guldin, P. Boldrighini, M. C. Orilall, U. Steiner, S. M. Gruner, U. Wiesner, *J. Mater. Chem. A* **2015**, *3*, 11478.

[42] P. C. A. Alberius, K. L. Frindell, R. C. Hayward, E. J. Kramer, G. D. Stucky, B. F. Chmelka, *Chem. Mater.* **2002**, *14*, 3284.

[43] E. L. Crepaldi, G. J. de, A. A. Soler-Illia, D. Grosso, F. Cagnol, F. Ribot, C. Sanchez, *J. Am. Chem. Soc.* **2003**, *125*, 9770.

[44] M. Nedelcu, J. Lee, E. J. W. Crossland, S. C. Warren, M. C. Orilall, S. Guldin, S. Hüttner, C. Ducati, D. Eder, U. Wiesner, U. Steiner, H. J. Snaith, *Soft Matter* **2009**, *5*, 134.

[45] H. N. Lokupitiya, A. Jones, B. Reid, S. Guldin, M. Stefik, *Chem. Mater.* **2016**, *28*, 1653.

[46] A. Alvarez-Fernandez, B. Reid, J. Suthar, S. Y. Choy, M. Jara Fornerod, N. Mac Fhionnlaoich, L. Yang, B. Schmidt-Hansberg, S. Guldin, *Nanoscale* **2020**, *12*, 18455.

[47] H. Zhao, T. Zhang, R. Qi, J. Dai, S. Liu, T. Fei, G. Lu, *Sens. Actuators, B* **2017**, *248*, 803.

[48] P. Innocenzi, A. Martucci, M. Guglielmi, A. Bearzotti, E. Traversa, *Sens. Actuators, B* **2001**, *76*, 299.

[49] X. He, W. Geng, B. Zhang, L. Jia, L. Duan, Q. Zhang, *RSC Adv.* **2016**, *6*, 38391.

[50] V. K. Tomer, P. V. Adhyapak, S. Duhan, I. S. Mulla, *Microporous Mesoporous Mater.* **2014**, *197*, 140.

[51] V. K. Tomer, S. Duhan, *Sens. Actuators, B* **2015**, *220*, 192.

[52] S. Jakhar, S. Duhan, S. Nain, *Mater. Res. Innovations* **2022**, *26*, 203.

[53] M. Groenewolt, T. Brezesinski, H. Schlaad, M. Antonietti, P. W. Groh, B. Iván, *Adv. Mater.* **2005**, *17*, 1158.

[54] S. Guldin, S. Hüttner, P. Tiwana, M. C. Orilall, B. Ülgüt, M. Stefik, P. Docampo, M. Kolle, G. Divitini, C. Ducati, S. A. T. Redfern, H. J. Snaith, U. Wiesner, D. Eder, U. Steiner, *Energy Environ. Sci.* **2011**, *4*, 225.

[55] N. Yamazoe, Y. Shimizu, *Sens. Actuators* **1986**, *10*, 379.

[56] K. A. Lantz, N. B. Clamp, W. van den Bergh, A. Sarkar, M. Stefik, *Small* **2019**, *15*, 1900393.

[57] Y. Deng, J. Wei, Z. Sun, D. Zhao, *Chem. Soc. Rev.* **2013**, *42*, 4054.

[58] A. Alvarez-Fernandez, B. Reid, M. J. Fornerod, A. Taylor, G. Divitini, S. Guldin, *ACS Appl. Mater. Interfaces* **2020**, *12*, 5195.

[59] J. Loizillon, B. Baumgartner, C. Sinturel, M. Abbarchi, B. Lendl, D. Grosso, *J. Phys. Chem. C* **2019**, *123*, 23464.

[60] T. Galy, M. Marszewski, S. King, Y. Yan, S. H. Tolbert, L. Pilon, *Microporous Mesoporous Mater.* **2020**, *291*, 109677.

[61] K. Ren, L. Huang, S. Yue, S. Lu, K. Liu, M. Azam, Z. Wang, Z. Wei, S. Qu, Z. Wang, *J. Mater. Chem. C* **2017**, *5*, 2504.

[62] Ravikant, S. S., G. Gupta, S. Yadav, P. K. Dubey, V. N. Ojha, A. Kumar, *Sens. Actuators, A* **2019**, *295*, 133.

[63] S.-F. Tseng, Y.-S. Tsai, *Appl. Surf. Sci.* **2022**, *606*, 155001.

[64] Nidhi, S. D., A. Kumar, S. Duhan, M. S. Goyat, *J. Mater. Sci.* **2022**, *57*, 3441.

[65] P. Innocenzi, P. Falcaro, J. M. Bertolo, A. Bearzotti, H. Amenitsch, *J. Non-Cryst. Solids* **2005**, *351*, 1980.

[66] N. A. Melosh, P. Lipic, F. S. Bates, F. Wudl, G. D. Stucky, G. H. Fredrickson, B. F. Chmelka, *Macromolecules* **1999**, *32*, 4332.

[67] M. Impéror-Clerc, P. Davidson, A. Davidson, *J. Am. Chem. Soc.* **2000**, *122*, 11925.

[68] D. Grosso, A. R. Balkenende, P. A. Albouy, A. Ayral, H. Amenitsch, F. Babonneau, *Chem. Mater.* **2001**, *13*, 1848.

[69] L. Vradman, L. Titelman, M. Herskowitz, *Microporous Mesoporous Mater.* **2006**, *93*, 313.

[70] K. Sen Chou, T. K. Lee, F. J. Liu, *Sens. Actuators, B* **1999**, *56*, 106.

[71] E. Poonia, M. S. Dahiya, V. K. Tomer, K. Kumar, S. Kumar, S. Duhan, *Phys. E* **2018**, *101*, 284.

[72] P. Qi, Z. Xu, T. Zhou, T. Zhang, H. Zhao, *J. Colloid Interface Sci.* **2021**, *583*, 340.

[73] B. Reid, I. Mane, F. Ahmed, M. J. Fornerod, M. Füredi, B. Schmidt-Hansberg, A. Alvarez-Fernandez, S. Guldin, *Microporous Mesoporous Mater.* **2022**, *345*, 112246.

[74] J. D. Bass, D. Grosso, C. Boissiere, E. Belamie, T. Coradin, C. Sanchez, *Chem. Mater.* **2007**, *19*, 4349.

[75] S. Alberti, P. Y. Steinberg, G. Giménez, H. Amenitsch, G. Ybarra, O. Azzaroni, P. C. Angelomé, G. J. A. A. de Soler-Illia, *Langmuir* **2019**, *35*, 6279.

[76] M. Matheron, T. Gacoin, J.-P. Boilot, *Soft Matter* **2007**, *3*, 223.

[77] Y. Yang, J. Li, H. Yuan, R. Carlini, X. Liu, *Mater. Chem. Phys.* **2022**, *280*, 125808.

[78] J. H. Anderson, G. A. Parks, *J. Phys. Chem.* **1968**, *72*, 3662.

[79] M. Pi, D. Wu, J. Wang, K. Chen, J. He, J. Yang, D. Zhang, S. Chen, X. Tang, *Sens. Actuators, B* **2022**, *354*, 131084.

[80] J. Zhu, N. Zhang, Y. Yin, B. Xu, W. Zhang, C. Wang, *Adv. Mater. Interfaces* **2022**, *9*, 2101498.

[81] X. Wang, J. hong Li, Y. Li, L. Liu, W. Guan, *Sens. Actuators, B* **2016**, *237*, 894.

[82] C. Boissiere, D. Grosso, S. Lepoutre, L. Nicole, A. B. Bruneau, C. Sanchez, *Langmuir* **2005**, *21*, 12362.

[83] P. Mezza, J. Phalippou, R. Sempere, *J. Non-Cryst. Solids* **1999**, *243*, 75.

[84] M. R. Baklanov, K. P. Mogilnikov, V. G. Polovinkin, F. N. Dultsev, *J. Vac. Sci. Technol., B: Microelectron. Nanometer Struct.–Process., Meas., Phenom.* **2000**, *18*, 1385.

[85] S. Brunauer, P. H. Emmett, *J. Am. Chem. Soc.* **1937**, *59*, 2682.

[86] M. Thommes, K. Kaneko, A. V. Neimark, J. P. Olivier, F. Rodriguez-Reinoso, J. Rouquerol, K. S. W. Sing, *Pure Appl. Chem.* **2015**, *87*, 1051.

[87] D. Babonneau, *J. Appl. Crystallogr.* **2010**, *43*, 929.